High-sensitivity CCD-based X-ray detector

Walter C. Phillips,[a]* Alexander Stewart,[a] Martin Stanton,[a] Istvan Naday[b] and Charles Ingersoll[a]

[a]Rosenstiel Basic Medical Sciences Research Center, Brandeis University, Waltham, MA 02454, USA, and [b]Argonne National Laboratory, Argonne, IL 60439, USA.
E-mail: phillips@brandeis.edu

The detector is designed for imaging measurements requiring relatively high sensitivity and high spatial resolution. The detector can discriminate single X-ray photons, yet has the wide dynamic range ($\sim$10000:1) associated with integrating detectors. A GdO_2S_2 phosphor screen converts the incoming X-ray image into an optical image. The optical image is coupled (without demagnification) to the CCD image sensor using a fiber optic faceplate. The CCD (Philips Semiconductors) has an area of 4.9 $\times$ 8.6 cm with 4000 $\times$ 7000 12 µm pixels. A single 12 keV X-ray photon produces a signal of 100 e^-. With 2 $\times$ 2 pixel binning, the total noise per 24 µm pixel in a 100 s image is $\sim$30 e^-, the detective quantum efficiency is $>$0.6 at 1 X-ray photon per pixel, and the full image can be read out in $<$4 s. The spatial resolution is 50 µm. The CCD readout system is fully computer-controlled, allowing flexible operation in time-resolved experiments. The detector has been characterized using visible-light images, X-ray images and time-resolved muscle diffraction measurements.

Keywords: detectors; X-ray detectors; X-ray diffraction; time-resolved diffraction; data acquisition.

1. Introduction

Most contemporary detectors designed for crystallography employ demagnifying optics to transfer the visible-light image formed by incident X-ray photons (xphs) to a CCD light sensor. These detectors are quite efficient at measuring diffraction peaks with thousands of xphs per pixel, so only incremental improvements in efficiency are possible in this intensity range. However, these detectors do not perform well at measuring signals with only tens of xphs per pixel. Our primary aim was to build a detector for measurements where typically the X-ray signal is weak, such as small-angle scattering, fiber diffraction or time-resolved diffraction measurements from muscle. For these measurements, improvements in efficiency of one or two orders of magnitude can be achieved. For measurements where the signal is strong, current CCD detectors typically saturate or bloom at 7–15 xphs per square micrometre of active area, whereas the detector described here saturates at 40 xphs per square micrometre, and does not bloom.

In general, it is impractical to build a CCD-based detector with a large area and very high sensitivity. Owing to the limited size of CCDs (typically 3–5 cm on a side), there is a necessary trade-off between area and sensitivity. For macromolecular crystallography, area is vital and sensitivity is less important. The most useful crystallography detectors have a large area, usually 20 $\times$ 20 cm or greater. We sacrificed area in order to gain sensitivity. In addition, experiments may require a detector with flexible operating modes, and we have incorporated this capability into our detector.

The detector uses a single large CCD (Philips Semiconductors type 7040) without the demagnifying fiber optic taper(s) or lens typically found in CCD-based crystallography detectors (Stanton *et al.*, 1994; Naday *et al.*, 1995; Suzuki *et al.*, 1999; Phillips *et al.*, 2000; Area Detector Systems, Poway, CA, USA; MAR, Evanston, IL, USA; Molecular Structure Corporation, The Woodlands, TX, USA). Demagnifying tapers or lenses that provide a large imaging area can transmit only a small fraction of the light from the X-ray-to-light converter to the CCD sensor. The Philips CCD has small pixels that provide high spatial resolution, a large electron storage capacity that provides a relatively large dynamic range, and an area of 4.9 $\times$ 8.6 cm. Similar CCD-based detectors without demagnifying tapers have been constructed, but these have smaller areas, lower dynamic range and less flexible image control (Eikenberry *et al.*, 1991; Smart Apex Detector, Bruker Nonius, Madison, WI, USA).

2. Description of the detector system

2.1. Basic design

The design objectives were to build a detector that would discriminate individual xphs, be mechanically simple, operationally stable, and controlled, as far as practical, by software in order to allow user control of operating modes. Fig. 1 shows a schematic cross-sectional drawing of the detector camera, and Fig. 2 shows a photograph of the camera and electronics.

X-ray photons are transmitted through a 0.25 mm-thick Be X-ray window and converted to light in a GdO_2S_2 phosphor sheet. Light is transmitted to the CCD through a fibre optic faceplate coupled to the front surface of the CCD. The X-ray converter sheet is held in contact with the faceplate by means of a sealed air-filled Mylar pillow that is compressed between the Be window and the faceplate. The CCD is cooled by a thermoelectric module (Melcor, Trenton, NJ, USA). Heat

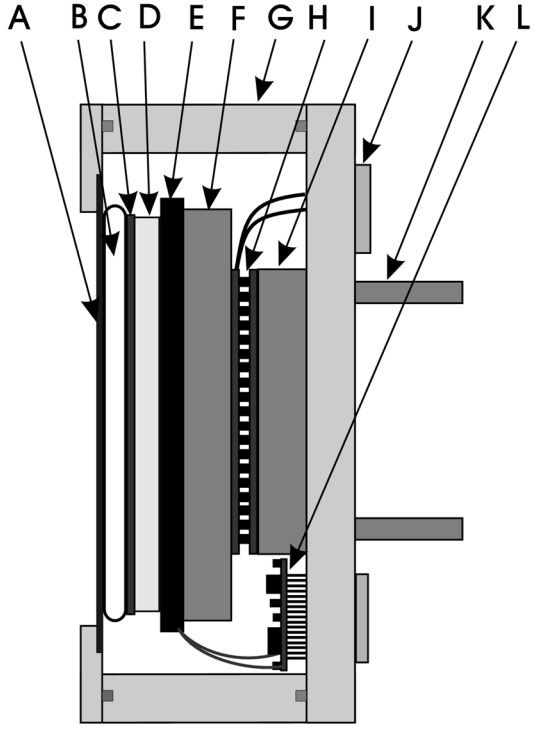

Figure 1
Schematic cross-sectional drawing of the camera: (A) Be window; (B) air-filled pillow; (C) X-ray-to-light converter; (D) fiber optic faceplate; (E) Philips 4000 $\times$ 7000-pixel CCD; (F) Cu heat-transfer block; (G) camera housing; (H) thermoelectric cooling module; (I) water-cooled heat exchanger; (J) electric feedthrough; (K) re-circulating chilled water; (L) preamplifier board.

is extracted from the module by a heat exchanger cooled by re-circulating water maintained at 277 K. The heat exchanger is sealed to prevent any water from entering the chamber. The converter, CCD, preamplifier, thermoelectric module and heat exchanger are mounted in a hermetically sealed light-tight chamber. The chamber is filled with dry nitrogen gas at the time of assembly, then sealed.

The CCD electronics are enclosed in a housing directly behind the camera. The electronics are controlled by a PC that configures all of the voltages and sends the full timing sequence to the electronics.

2.2. CCD and X-ray converter

The Philips FTF7040 CCD (Narragansett Imaging, Slatersville, RI, USA) has 4096 × 7168 12 µm pixels with a full well value of ∼600 ke$^-$. The CCD has four amplifiers and two serial registers, and incorporates vertical anti-blooming (Janesick, 2001*a*). The large full well results in a relatively large dynamic range, even though the signal/X-ray is ∼100 e$^-$. The sensor is permanently coupled to a fiber optic faceplate with 6 µm-diameter fibers (type 47A, Schott Fiber Optics, Southbridge, MA, USA). The X-ray converter is a 13 mg cm^{-2} (45 µm-thick) layer of Gd_2O_2S:Tb, prepared by settling Gd_2O_2S:Tb (Nichia America, Lancaster, PA, USA) and an organic binder in an organic solution onto a 25 µm-thick aluminized-Mylar sheet (Gruner *et al.*, 1993).

2.3. Temperature control

Thermally induced leakage current accumulating in the pixel array generates a 'dark-current image', *i.e.* an image is formed even though no light is incident on a CCD. The dark image can be measured and subtracted from data images, but the Poisson noise associated with the dark current contributes to the total image noise. To minimize the effect of the dark current, scientific CCD chips are cooled. For the Philips CCD, the dark current doubles every 6 K. The dark current in our detector is greater than in most other CCD-based detectors because (i) we are cooling only to 238 K and (ii) Philips CCDs are not run in 'MPP mode' (Janesick, 2001*b*). These factors make it necessary to regulate the CCD temperature to within 0.1 K in order that the dark-current image can be accurately measured. In addition, the CCD temperature must be changed slowly in order to prevent damaging the device by disrupting the CCD-to-faceplate and CCD-to-substrate bonds.

To meet these goals we developed a fail-safe computer-based temperature control system from commercially available subsystems. A dedicated PC runs the program controlling the thermoelectric power supply, maintaining the CCD temperature to within 0.1 K, and ramping the temperature up or down at 1.5 K min^{-1} when warming up or cooling down the CCD, both in routine operation or in the event of a power failure, water re-circulator failure *etc*. The program checks whether the current system state is following the expected trajectory in terms of CCD temperature, heat-exchanger temperature, UPS status, power output *etc*. When a failure or an unexpected event causes the system to vary from its expected trajectory, the response of the controller is to ramp the thermoelectric power supply current down to zero using a pre-programmed sequence.

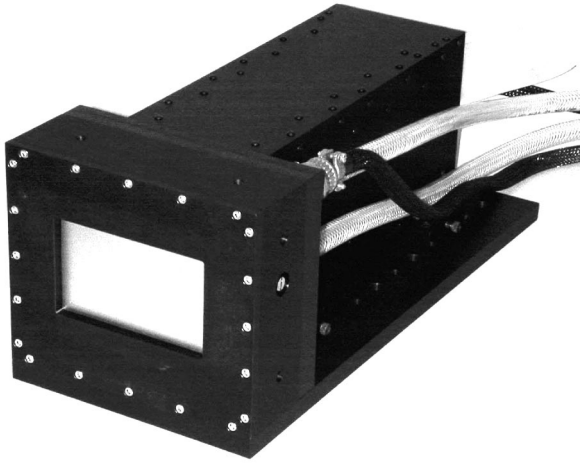

Figure 2
Photograph of camera and electronics. The camera is 16.5 cm (W) × 15 cm (H) × 7.6 cm (D), and the electronics extend back 30 cm from the camera. The Be window covers the imaging area. All the control and data signals are carried by the two 68-pin ribbon cables at the back of the electronics enclosure, re-circulating water by the two reinforced plastic hoses, and the temperature monitoring and thermoelectric power signals by the black cable attached to the back of the camera.

2.4. Electronics

The electronics supporting the CCD are designed as a set of modules that can be used to run any CCD. The system consists of eight printed circuit boards mounted on a mother board, and a CCD-dependent socket board for mounting the CCD itself. Every parameter of the CCD operation is accessible to software. The electronics are mounted directly behind the camera.

CCD systems require that complex patterns of voltages be applied to the device electrodes (the clocking sequence; Janesick, 2001*c*). In this design we have implemented a conceptually simple system in which the clocking sequence is generated directly from the memory of a Windows PC by a PCI card (National Instruments PCI-DIO-32HS). We have full control of the CCD operating modes. This is in contrast to other CCD-based X-ray detectors, in which the sequencing is basically hard wired. The flexibility provided by the computer control was essential for the development of the detector because it allowed us to rapidly investigate a large number of timing and voltage parameters. The computer control now provides the user with a practical method for operating the CCD in various ways appropriate for different kinds of measurements.

The digital clocking sequence is fed through a field-programmable gate array (FPGA) to the CCD clock drivers. The output voltage levels to the CCD chip are controlled with digital-to-analogue converters (ADCs), as are the gains and offsets for the CCD output signals. The distributed impedance associated with the 4.5 cm length of the parallel electrodes on the Philips 7040 CCD necessitates multilevel clocking to achieve good charge transfer efficiency (CTE) across the whole device. The parallel output drivers employ fourth-order analogue filters for clock waveform shaping. The serial output drivers have two programmable levels and use simple R–C shaping. The CCD output signals are processed by a double-correlated double-sampling circuit (DCDS) and digitized at 1 MHz. The pixel data are buffered by a 4K FIFO memory and read directly into the PC system RAM using a second PCI card.

2.5. Software

The software is based on a client–server scheme: the server system manages the detector hardware using a dedicated computer, and the user-interface client can run on any PC. The detector computer accepts text-based commands across the network using a secure protocol. The computer continually outputs the digital sequence for clocking the CCD in real time at 10 MHz, receives image pixels, and buffers the incoming image frames.

The software was developed using well supported commercial interface hardware (National Instruments) and the Borland Delphi development environment for Windows 2000. There are four main modules to the detector control software: sequencing, pixel input, CCD voltage settings, and network communication. Multiple high-priority threads and non-paged memory buffers for the pixel and sequence data are used to ensure that sequencing and pixel input are not impeded by other process activity on the computer.

A Windows-based user control program integrates with synchrotron beamline operation (shutters, beam-current monitors *etc*). This program gives immediate access to images, contains simple on-line analysis tools, and allows selection of binning and exposure modes. The CCD sequence is generated from the user's binning-mode selection. (CCD voltage and CCD sequence editor programs are available for those who want to edit the sequence directly.) The program corrects images on the fly for non-uniform response introduced by the converter, faceplate and CCD, and subtracts a dark-current image. The full correction process takes <1 s. Because it is impractical to collect non-uniform response correction images for each possible binning mode, the correction image for any particular binning mode is generated from a limited number of reference correction images by binning the reference image in software to match the chosen binning mode.

The dark-current reference images are made using a median-of-three technique in order to reduce random noise and avoid recording cosmic-ray events and events generated by radioactive impurities in the fibre optic. Multiple dark-current images of differing duration can be interpolated to avoid the need for taking reference dark images for each exposure time used.

2.6. Pixel binning and sub-region readout

The 16-bit ADC digitization rate is 1 MHz (1 Mpixels s^{-1}); thus it takes 7 s to read out the full unbinned image with four readout channels. Readout time is reduced when the pixels are binned on the chip before readout. The time required to read out an image frame is

$$\text{(Parallel frame time)} + \text{(No. parallel lines)} \times \text{(serial-line read time)}. \quad (1)$$

The fastest parallel frame time is 1 mm ms^{-1} (25 ms to parallel shift the whole image into the two serial registers). The full number of parallel lines is 4000 (2000 when reading from both serial registers). The time to read out one full line (3500 pixels) from the serial register (serial line time) is 3.5 ms. Serial binning can only reduce this by $\sim$40% because the serial base clock is currently fixed at 10 MHz.

The programmable controller allows sub-regions to be read out in several ways. For example, the time to read a 1×1 cm masked-off sub-region, binned 4×4 pixels, is $10 + (10000/12) \times 200 \times 10^{-6} =$ 177 ms. Because of serial binning, this can be reduced to $\sim$130 ms.

Since all the signals are independently programmable, the upper and lower halves of the sensor can be clocked separately. By binning from one half of the sensor into the other half, several binned frames can be stored rapidly without serial transfers. Once the binned frames fill the frame-store region, the imager is read out in the normal way. This allows finer time resolution than simple framing or streak-camera modes, since serial line readout is deferred until the frames have been collected.

3. Characterization

3.1. Calibration

The flood-field calibration images needed for correcting non-uniform response were collected by setting the detector at 1.5 m from the filtered point source of an Mo-target rotating-anode generator operating at various excitation voltages. The corrections are accurate (preserve intensity information) to better than 1%. Because the fibre optic faceplate is essentially free of spatial distortions, no corrections for spatial distortion are applied to the images. Thus, pixel re-binning is not required, and the full spatial resolution of the image is preserved.

3.2. Spatial resolution

Spatial resolution was measured with visible light (without the X-ray converter) and with X-rays (with the X-ray converter). The resolution measured with the converter is considerably poorer than that measured without the converter, demonstrating, as expected, that light scattering in the converter is the primary determinant of spatial resolution.

Fig. 3 shows an image, and image enlargements, of an optical resolution line-pair test target, made at full resolution (12 μm pixels). The modulation contrast at the Nyquist frequency (42 line-pairs mm^{-1}) is >60%, as can be seen in Fig. 3(*d*). While the resolution is degraded somewhat because the pixel size is only twice the diameter of the optical fibers, the detail in the image shows that the coupling between the faceplate and the CCD does not significantly degrade the resolution.

The X-ray line spread function (LSF) was measured with a 12 keV X-ray flood field and a 12 μm-wide Ta slit placed on the Be window at an angle of $\sim 1^\circ$ with respect to the CCD pixel array, with 2×2 pixel binning (Fujita *et al.*, 1992). The LSF was generated from the slit image (Fujita *et al.*, 1992). The full widths at 50%, 10%, 1% and 0.1% of the maximum are 50 μm, 120 μm, 240 μm and 720 μm, respectively. The modulation transfer function (MTF) was calculated from the Fourier transform of the LSF. Fig. 4 shows the measured LSF and the corresponding (pre-sampled) MTF.

3.3. Gain and noise

The conversion gain, determined from the measured photon transfer curve, is 10 e^- per analog-to-digital unit (ADU) (measured with light; Janesick, 2001*d*). The X-ray gain for 12 keV xphs, measured using the beam from an Ag-target X-ray generator, is 10 ADU xph^{-1}, or 100 e^- xph^{-1}. For these measurements, the beam was filtered (and attenuated) by multiple sheets of X-ray film. The average X-ray energy in the beam, measured with an energy-sensitive CdZnTe detector (Amptek, Bedford, MA, USA) was 12 keV. The count rate through a 1 mm-diameter hole was measured with a calibrated NaI/photomultiplier counter, then the intensity through the pinhole was recorded with the detector. The intensity was determined by integrating over an area somewhat large than the hole diameter.

The contributions to the noise from the readout and the dark current were measured by taking sets of dark-current images for a series of integration times and temperatures. The read noise is 1.4 ADU $pixel^{-1}$, independent of the pixel binning ratio used. The dark current at 240 K is 0.16 ADU $pixel^{-1}$ s^{-1} for 12 μm pixels and 0.6 ADU $pixel^{-1}$ s^{-1} for 2×2 binned pixels *etc.* The dark noise equals the standard deviation in the dark current. The total noise in a 4×4 binned pixel is approximately equal to the signal generated in the pixel by a single 12 keV xph (for short exposures). Fig. 5 shows an example of a low-flux image, where the array of holes in a mask can be seen by eye in this 10 s exposure with an average of 5 xphs $hole^{-1}$.

3.4. Response linearity

The response of the detector was measured by collecting a series of images with visible light. Based on our experience with phosphor converters (and on the physics of these phosphors), we know that the response of the X-ray converter is linear at the X-ray fluxes at which this detector will be used. Thus, we only needed to measure the response linearity of the CCD and the electronics. This is most accurately performed with light. To make the measurements, we replaced the Be window with a transparent plastic window, and placed a light-tight shroud over the detector. An LED mounted inside the shroud illuminated the CCD. The exposure was determined by controlling the number of LED flashes and the flash duration. One flash corresponded to less than 1 ADU; an exposure of ∼100000 flashes saturated the CCD output. The light output of the flashes was reproducible within our measurement accuracy.

The CCD control voltages and sequence timing were adjusted to produce a nominally linear output. A series of images with exposures from very low to saturation were made. By dividing sets of these images, we could measure linearity over the entire dynamic range of the sensor (10 ADUs–64000 ADUs). We found that the system

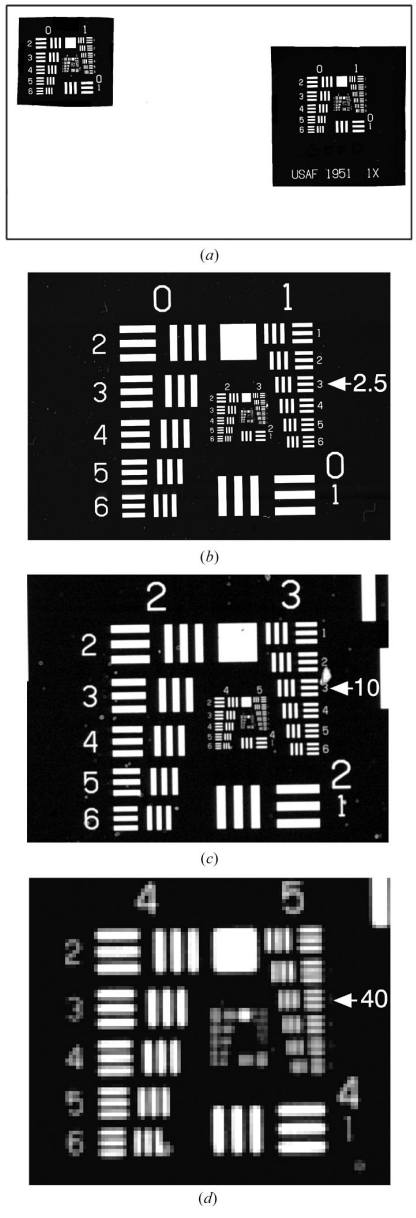

(*a*)

(*b*)

(*c*)

(*d*)

Figure 3
Visible-light image of a line-pair test target. (*a*) Full CCD imaging area (49 × 86 mm) with two test targets; (*b*) right-hand target magnified; (*c*) center area of the target magnified; (*d*) center area of the target magnified further. The figure scales, in line-pairs mm^{-1}, in (*b*), (*c*) and (*d*) are indicated by arrows next to the corresponding six-line groups. No calibrations or corrections have been applied to the image, made with 12 μm pixels.

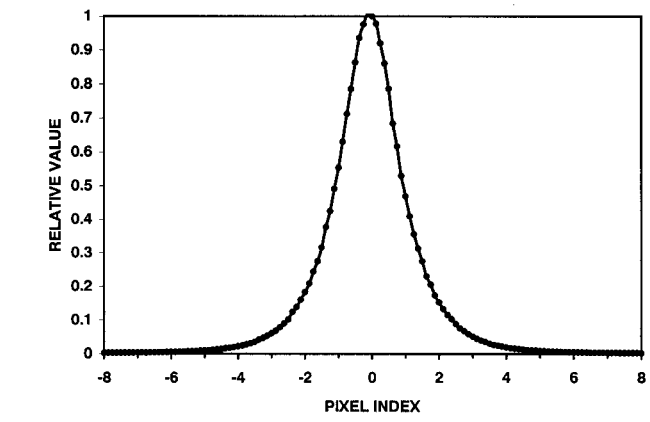

(*a*)

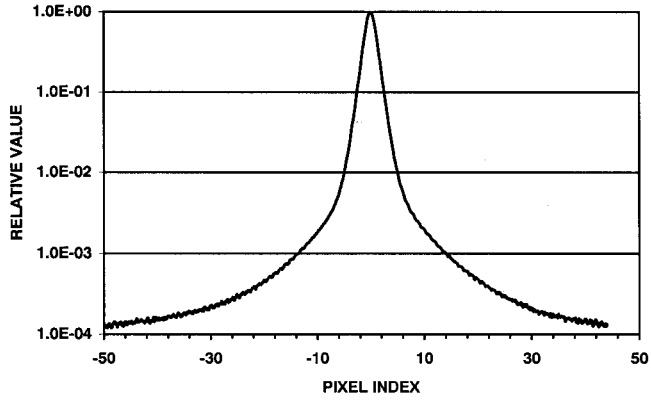

(*b*)

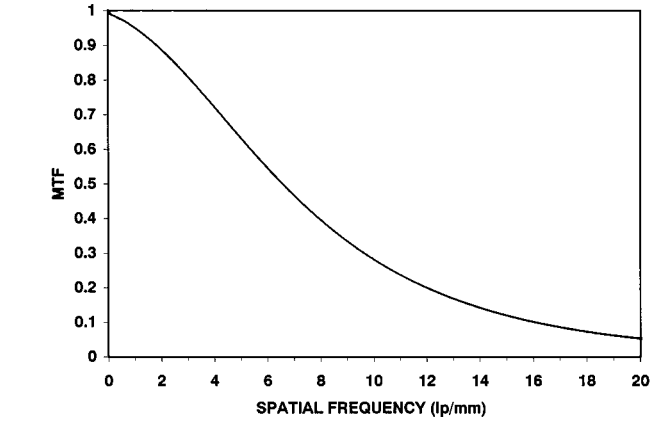

(*c*)

Figure 4
The measured LSF plotted on (*a*) a linear scale and (*b*) a logarithmic scale, and (*c*) the pre-sampled MTF derived from the LSF. The pixel size for these measurements is 24 μm.

is linear to within 1% over the full range, over the full area of the sensor.

3.5. Dynamic range

The dynamic range (DR) is often defined as the ratio of the largest signal that can be measured to the noise per pixel. This definition is not necessarily a practical one, because the signal from a single xph will be spread out over many pixels. For this detector, the signal will be spread out into ~100 12 μm pixels. The read noise in a pixel, unbinned or binned, is smaller than the signal from an X-ray photon, and for relatively short exposures (10 s) the dark-current noise in a 12 μm pixel (or 4 × 4 binned pixel) is also less than the signal from an X-ray photon. Therefore, we will consider the DR as the ratio of the largest signal (the full well signal), *i.e.* 6400 12 keV xphs, to the signal from 1 xph. Then, ignoring the signal spreading, the detector has a DR of 6400. The finite capacity of the serial and summing registers limits the DR for binned pixels. For this CCD, the serial register holds $\sim 1.2 \times 10^6$ electrons and the summing well holds $\sim 3 \times 10^6$ electrons = 30000 xphs. For 2 × 2 pixel binning, the DR is 4 × 6400. For 3 × 3 or 4 × 4 or 10 × 10 binning, the DR is also 26000 (providing the integration is short enough that the dark noise is not significant). The DR will be less for longer exposures. For example, for a 1000 s exposure and 4 × 4 pixel binning the DR, calculated from the measured noise per pixel, is 26000/2.5 $\simeq$ 10000.

3.6. Detective quantum efficiency (DQE)

For an ideal detector (one in which every incident xph creates a signal and there is no intrinsic noise), DQE = 1.0. For a real detector, DQE < 1 because not every incident xph is detected, and because there is always some detector noise. The $(\mathrm{DQE})^{-1}$ represents how many xphs are required to produce an output signal uncertainty equivalent to that of an ideal detector. The DQE is defined as

$$\mathrm{DQE}(f) = \frac{\left|\mathrm{MTF}(f)\right|^2}{Q_{\mathrm{in}}\,\mathrm{NPS}(f)}, \qquad (2)$$

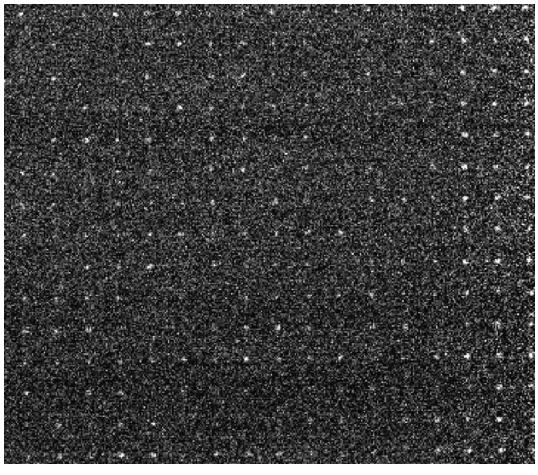

Figure 5
Mask image made with 10 keV incident X-ray photons and 4 × 4 pixel binning. The mask holes are 0.15 mm in diameter spaced 1 mm apart. There are 5 xphs hole^{-1} in the 14 columns on the left and about 12 xphs hole^{-1} in the three columns on the right.

where Q_{in} is the incident X-ray flux (xphs mm^{-1}) and NPS(f) is the noise power spectrum (Shaw, 1963, 1975; Wagner & Muntz, 1979). At zero frequency, this expression reduces to

$$\mathrm{DQE}(0) = \frac{T_w}{1 + R_s + R_{\text{X-ray}} + 1/G + A(n_r + N_d t)/(I T_w G^2)}, \qquad (3)$$

where T_w is the product of the phosphor absorption efficiency and the window transmission (Be plus Mylar pillow plus Mylar), R_s is the phosphor noise factor (typically ~0.15), $R_{\text{X-ray}}$ represents the variance introduced by the range of wavelengths in the X-ray beam (Nishikawa & Yaffe, 1985; Hillen *et al.*, 1987), G is the detector gain, A is the pixel area, n_r is the variance in the read noise, N_d is the variance in the dark current, t is the integration time, and I is the number of incident xphs in area A (Stanton *et al.*, 1992). N_d is not measured directly, but can be deduced from the dark current since dark-current generation is a Poisson process.

The measured DQE for 2 × 2 binned pixels for 100 xphs pixel^{-1} and 1 xph pixel^{-1} are plotted in Fig. 6. The DQE was obtained from the measured NPS and measured MTF. These were measured with the filtered flood beam from an Ag-target generator, as described above. The number of xphs per pixel was measured with an NaI/photomultiplier counter. DQE(0) is in good agreement with that calculated from equation (3), using values measured for the filtered flood spectrum: T_w = 0.832 (transmission of window = 0.978, transmission of the Mylar pillow = 0.991, absorption of the 13 mg cm^{-2} phosphor = 0.858), $R_{\text{X-ray}}$ = 0.074 (calculated for the spectrum we used), G = 100 e^- xph^{-1}, A = 2 × 2 pixels, n_r = 200 e^-, N_d = 8 e^- $(10\ \mathrm{s})^{-1}$ and t = 10 s. Using these parameter values, the maximum value ($I \simeq 10^4$) for DQE(0) is 0.67.

4. Diffraction results

For an initial test of the detector, diffraction patterns from live American grass frog sartorius muscle were recorded at the APS BioCAT beamline. The muscle (in oxygenated Ringers solution at 282 K) was electrically stimulated with alternating 3 ms pulses (10 V cm^{-1}) at 50 Hz for 3 s to cause maximal contractile force to develop.

Data were collected with a 100 × 300 μm beam (size at specimen), a flux of $\sim 10^{13}$ xphs s^{-1} at 13 keV, and a 2 m evacuated flight tube between the specimen and the detector. Fig. 7 is a reference image

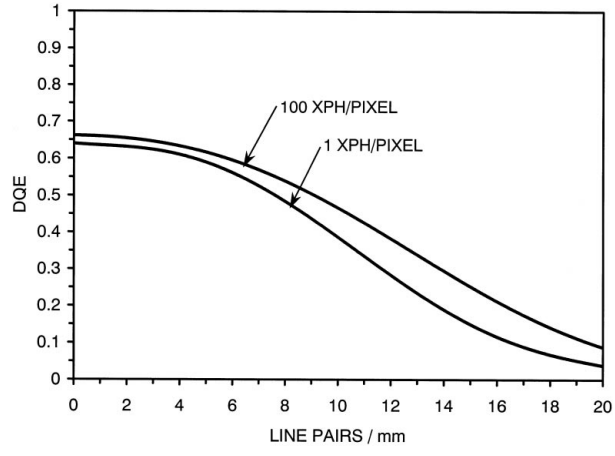

Figure 6
The DQE, measured at 12 keV for 2 × 2 pixel binning (24 μm pixels, corresponding Nyquist frequency 21 line-pairs mm^{-1}).

that shows a full pattern from a contracting muscle collected in 1 s with pixels asymmetrically binned 2 × 16 (24 × 192 μm) on the CCD. The detector faithfully records the entire pattern out to 27.5 Å, demonstrating the dynamic range of the detector. Using previous detector systems, we were unable to obtain accurate measurements from the weak outer reflections without saturating the stronger inner reflections. Fig. 8 shows the 28 Å and 27.5 Å reflections in a 1 s exposure, with pixels binned 4 × 32 (48 × 384 μm). There are ∼1000 xphs in the stronger peak. The outer 28 Å and 27.5 Å meridional reflections were used to measure the elastic changes in the myosin and actin protein filaments during muscle contraction at maximum tension. (27.5 Å is the axial rise of subunits along the helical actin filaments, and the 28 Å reflection is the 15th order of the myosin filament axial repeat.)

The inner reflections (145 Å) were used to investigate the change in orientation of the myosin cross-bridges caused by the biochemical and mechanical events following a rapid change in muscle length and tension. These experiments are part of a project to understand the fundamental mechanism of muscle contraction in terms of the known molecular structures of actin and myosin. We are attempting to measure myosin head cross-bridge orientation in active muscle following rapid shortening of a contracting muscle.

A servomotor-controlled lever synchronizes the myosin head motions by controlling the length of the muscle. This lever applies rapid shortening steps (quick releases) to the contracting muscle. A quick release causes the tension in the muscle to fall, and this allows the myosin head cross-bridges attached to actin filaments to undergo a single mechanical and enzymatic cycle. As soon as the length step is completed, the shutter is opened for 2 ms, a diffraction pattern is recorded, then the shutter is closed. The biochemical and mechanical events following the length step are over in a few ms. The muscle is then stretched back to its initial length. The cycle is repeated a number of times for length steps of different sizes at intervals of 100 ms. The electrical stimulation of the muscle lasts for 2.5 s. Peak contraction occurs for a little over 2 s, allowing 20 length step cycles to be performed. A group of ten different step lengths is applied, and then repeated to control for any changes between the start and the end of the contraction. The muscle is allowed to relax for several minutes before it is translated so that the beam strikes an unirradiated volume, and the measurement cycle is repeated. For living muscle, irreversible damage occurs after a few tens of milliseconds of such exposure to the synchrotron beam. In this experiment, each contraction of the muscle gave a full set of data.

Fig. 9 shows a series of exposures from a single 2 s contraction of a sartorius muscle. The detector surface was masked with a 9 mm-high slot that allowed the meridional reflections to be recorded. Twenty sequential 'streak-camera' exposures were recorded with the shutter open for 2 ms and closed for 100 ms. Two groups of ten quick-release cycles of the muscle are recorded in the 20 exposures comprising this image, as described above. The quick-release muscle length step was increased monotonically in each series of exposures (from right to left in Fig. 10). The recorded data were shifted vertically on the CCD at a rate of 10 mm per 100 ms, allowing sequential exposures to be recorded without overlap. Each pixel represents the intensity in a 32 × 2 binned pixel (384 × 24 μm). The circular beam stop appears elliptical due to the asymmetric binning. The changes in the position, intensity and shape of the 145 Å reflection provide information about cross-bridge movement.

Fig. 10(*a*) shows a magnified area of the previous image around the 145 Å reflection. There are ∼800 xphs in the weakest peak. By eye, the peak appears relatively weak because there are 3 xphs pixel^{-1} in the background under the peak, and the peak is spread out over ∼700 pixels. The shape of the reflection can be seen more clearly in Fig. 10(*b*), which shows the sum of 20 image frames. The splitting of the reflection is caused by interference between the two halves of the myosin filament, providing phase information that can be used to interpret cross-bridge motion. These figures illustrate the advantage of the asymmetric 32 × 2 binned pixels (384 × 24 μm). If a detector with square 24 μm pixels had been used, the signal from each pixel would have been spread out over 16 symmetrical pixels, causing the average signal per pixel to be less than 0.15 xphs, whereas a larger

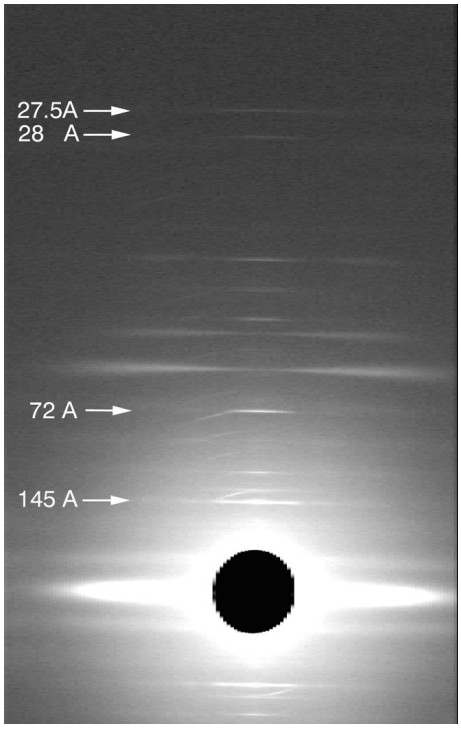

Figure 7
Diffraction pattern from frog muscle, 1 s exposure at 13 keV, measured with asymmetric 2 × 16 pixel binning. The full dynamic range in the image cannot be displayed in the print.

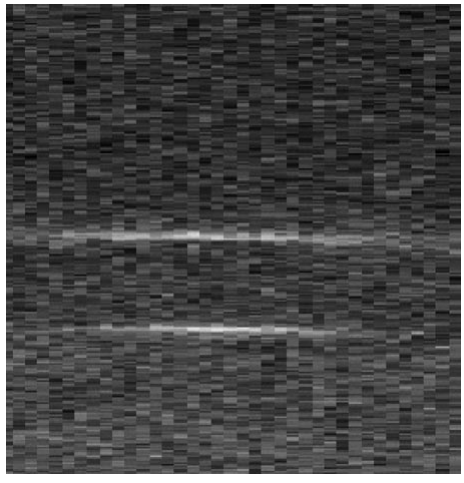

Figure 8
28 Å and 27.5 Å reflections from frog muscle, recorded with 4 × 32 pixel binning. The weaker peak represents 500 13 keV xphs.

symmetrical pixel would not adequately resolve the axial structure in the reflection.

5. Radiograph

Fig. 11 is included to demonstrate the routine imaging capabilities of the detector. The flower petals attenuate the beam by ∼4%. Detail in the petals is clearly seen in the image.

6. Discussion

The signal from each xph is ∼3 times the noise (for short exposures). Thus the sensitivity approaches that of a multiwire detector, yet this detector has considerably better spatial resolution, many image-collection options, high count-rate capability, and greater operational simplicity and reliability than a multiwire detector.

The DQE and spatial resolution of the detector are limited primarily by the phosphor converter. For the current Gd_2O_2S converter, the thickness of ∼45 μm limits the X-ray absorption at 12 keV to ∼82%, and the FWHM of the PRF to ∼60 μm. A thinner converter would decrease the DQE, but improve the spatial resolution. A CsI converter might improve both. The DQE is also limited by the phosphor noise factor. However, even with these limitations, DQE(0) $\simeq 0.65$ for 12 keV xphs at 1 xph (50 μm pixel)$^{-1}$ (30 s)$^{-1}$. For a typical CCD-based detector designed for crystallography, DQE(0) $\simeq$ 0.01 at 1 xph pixel^{-1}, and $\simeq$ 0.1 at 100 xph pixel^{-1} (Phillips *et al.*, 2000).

Two inherent properties of this CCD are important for our application: the relatively small (12 μm) pixels, and the large pixel full well (∼600 ke$^-$). The small pixels allow multiple asymmetric binning patterns. The large full well provides a large dynamic range.

Every signal in the digital sequence for clocking the CCD is accessible from a 'point-and-click' interface. Both the temporal pattern and the voltage range can be adjusted for each CCD clocking signal. Different sequences can be engaged and edited on the fly during operation. This avoids the sequence compiling and download processes associated with DSP or logic-based solutions. The dedicated detector computer continually outputs the full sequence in real time to the electronics. This capability facilitated the development of the hardware and software, and allows the user to define and select operating parameters and modes.

For the muscle measurements, the high signal per X-ray photon made individual millisecond exposures statistically viable, and the flexible 'streak-camera' mode of operation enabled data collection of multiple time events during a single contraction. Similar measurements at higher time resolution (Lombardi *et al.*, 1995) have been carried out using the Daresbury gas-filled area detectors (Lewis *et al.*, 1992) which are somewhat more complex than the current system. The experimental requirements of the multiple short exposures in a single 2 s contraction made the muscle experiment a demanding test of the detector. Using an unconventional operating mode, which had

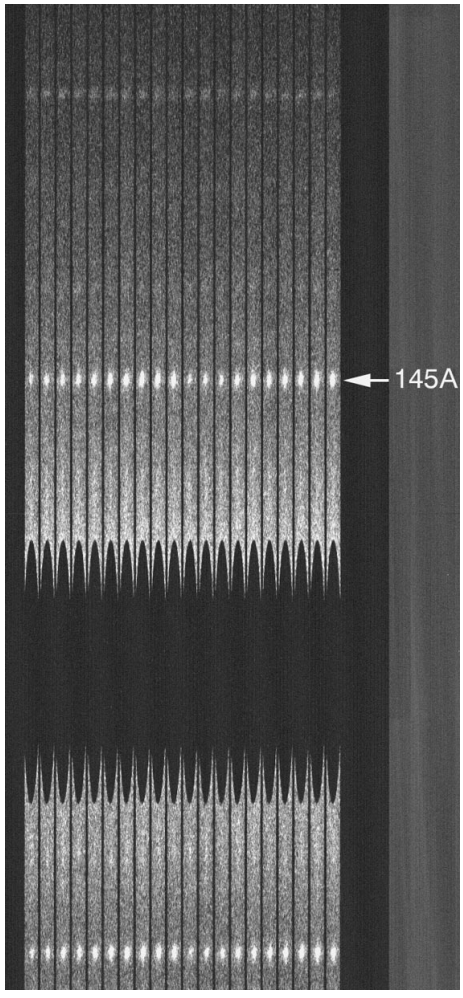

Figure 9
Twenty 2 ms exposures from frog muscle, made with a 9 mm slit in front of the detector, with 32 × 2 pixel binning.

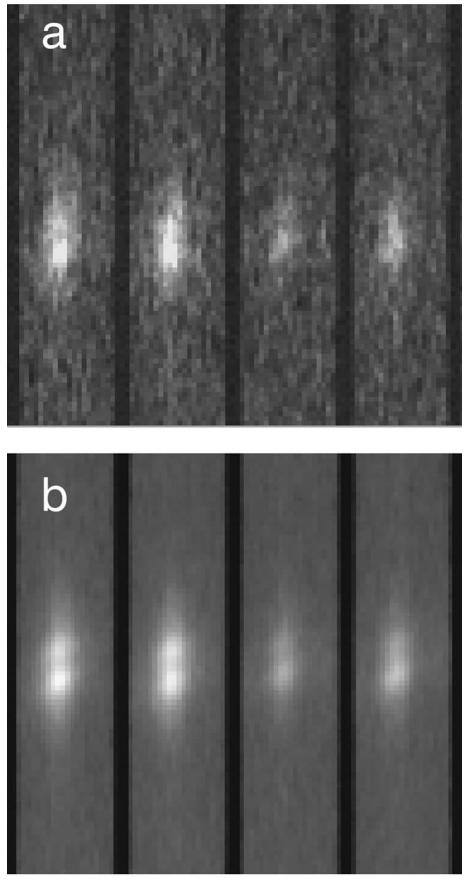

Figure 10
(*a*) Area of the image in Fig. 9, showing four sequential 2 ms exposures for the 145 Å reflection. (*b*) Addition of 20 data frames.

Figure 11
Radiograph of a daffodil recorded at 13 keV with 2 × 2 pixel binning and 5000 incident xphs per pixel.

asymmetric pixel binning and provided frame store on the CCD, the same volume of muscle could be studied in a series of exposures in one experiment before the tissue was destroyed by the intense beam. Previous protocols measured only one size of length step in a single contraction because the signal had to be integrated to overcome the read noise of previous detector systems. The muscle was destroyed by the beam before the measurements were completed, requiring several muscle samples for the measurement sequence. It was difficult to control for factors such as muscle fatigue and radiation damage, thus significant uncertainty was introduced into the results.

The greatest limitation of the detector is its relatively small area. The detector area could be increased by a factor of two in a straightforward way by using two identical 49 × 86 mm CCDs and two additional fiber optic faceplates. The faceplates could be cut in such a way that they would join at the input surface to form a continuous 98 × 86 mm area, and they would separate at the exit surface to allow a gap between the sensors to accommodate the packaging margin of the CCDs. Alternatively, a short fiber optic taper with a demagnification ratio of 5–10% could be used on each CCD. This scheme would allow any number of CCDs to be incorporated into an array.

The muscle diffraction data were collected in collaboration with Professor Hugh Huxley of Brandeis University, whose expertise was essential to this project. We thank Dr Huxley for permission to show his results, Mr Tao Wu for measuring the DQE, and Dr Thomas Irving, director of BioCAT, for assisting with data collection. Funding for this project was provided by the NIH, grant RR-12598-03.

References

Eikenberry, E., Tate, M., Belmonte, A. L., Lowrance, J. L., Bilderback, D. & Gruner, S. M. (1991). *IEEE Trans. Nucl. Sci.* **38**, 110–118.
Fujita, H., Tsai, D., Itoh, T., Doi, K., Morishita, J., Ueda, K. & Ohtzuka, A. (1992). *IEEE Trans. Med. Imag. II*, **1**, 34–39.
Gruner, S. M., Barna, S. L., Wall, M. E., Tate, M. W. & Eikenberry, E. (1993). *Proc. Soc. Photo-Opt. Instrum. Eng.* **2009**, 98–108.
Hillen, W., Schiebel, U. & Zaengel, T. (1987). *Med. Phys.* **14**, 744–751.
Janesick, J. R. (2001*a*). *Scientific Charge Coupled Devices*, Vol. PM83, p. 304. Bellingham, WA: Society for Photo-Optical Instrumentation Engineers.
Janesick, J. R. (2001*b*). *Scientific Charge Coupled Devices*, Vol. PM83, pp 310–318. Bellingham, WA: Society for Photo-Optical Instrumentation Engineers.
Janesick, J. R. (2001*c*). *Scientific Charge Coupled Devices*, Vol. PM83, pp. 37–42. Bellingham, WA: Society for Photo-Optical Instrumentation Engineers.
Janesick, J. R. (2001*d*). *Scientific Charge Coupled Devices*, Vol. PM83, pp. 97–107. Bellingham, WA: Society for Photo-Optical Instrumentation Engineers.
Lewis, R. A., Fore, N., Helsby, W., Hall, C., Jones, A., Parker, B., Sumner, I., Worgan, J. S. & Budtz-Jørgensen, C. (1992). *Rev. Sci. Instrum.* **63**, 642–647. (http://detserv1.dl.ac.uk/Herald/detectors_rapid.htm.)
Lombardi, V., Piazzesi, G., Ferenczi, M. A., Thirlwell, H., Dobbie, I. & Irving, M. (1995). *Nature (London)*, **374**, 553–555.
Naday, I., Ross, S., Kayno, M., Westbrook, M. L., Westbrook, E., Phillips, W. C., Stanton, M. & O'Mara, D. (1995). *Proc. Soc. Photo-Opt. Instrum. Eng.* **2415**, 236–249.
Nishikawa, R. M. & Yaffe, M. J. (1985). *Med. Phys.* **12**, 32–39.
Phillips, W. C., Stanton, M., Stewart, A., Qian, H., Ingersoll, C. & Sweet, R. M. (2000). *J. Appl. Cryst.* **33**, 243–251.
Shaw, R. (1963). *J. Photogr. Sci.* **11**, 199–204.
Shaw, R. (1975). *Proc. Soc. Photo-Opt. Instrum. Eng.* **70**, 359–363.
Stanton, M., Phillips, W. C., Li, Y. & Kalata, K. (1992). *J. Appl. Cryst.* **25**, 638–645.
Stanton, M., Phillips, W. C. & O'Mara, D. (1994). *Soc. Photo-Opt. Instrum. Eng.* **2278**, 16–20.
Suzuki, M., Yamamoto, M., Kumasaka, T., Sato, K., Totokawa, H., Aries, I. F., Jerram, P. A., Gillick, D. & Ueki, T. (1999). *J. Synchrotron Rad.* **6**, 6–18.
Wagner, R. F. & Muntz, E. P. (1979). *Proc. Soc. Photo-Opt. Instrum. Eng.* **173**, 162–165.

 Received 27 September 2001 • Accepted 22 November 2001